

Improved inductance calculation in variable power inductors by adjustment of the reluctance model through magnetic path analysis

Sarah Saeed, *Student Member, IEEE*, Jorge Garcia, *Member, IEEE*, Marina S. Perdigão, *Member, IEEE*, Valter S. Costa, *Student Member, IEEE*, Bruno Baptista, and André M. S. Mendes, *Member, IEEE*

Abstract— This paper presents a study to improve the inductance calculation of magnetic components in power converters, of particular interest in the case of applications using variable inductors. In order to increase the accuracy of the estimation of the reluctance paths, several factors have been taken into consideration, such as: the permeability definition under saturation, the temperature effect on the magnetic material behavior and the distribution of saturated regions in the magnetic core. The methodology of the present study is to compare the analytical models derived from circuitual equivalents against Finite Element Analysis numerical techniques, in order to validate the proposed model of a variable inductor, including the effects of the mentioned factors. The proposed model is then compared with experimental measurements to prove its validity. Finally, a design example for the variable inductor is presented.

Index Terms—FEA modeling, variable inductor, reluctance circuit, permeability, controlled saturation, core temperature.

I. INTRODUCTION

THE accurate estimation of the inductance value of a magnetic device is an essential need in order to achieve a better performance in a power electronic converter. Therefore, it is necessary to develop an accurate model of the magnetic device as well as the study of the limitations of its design such as material saturation, core losses, etc.

Manuscript submitted April 24, 2020; revised August 5, 2020 and October 25, 2020; accepted November 22, 2020. Paper 2020-IPCC-0608.R2, presented at the 2019 IEEE Energy Conversion Congress and Exposition, Baltimore, MD USA, Sep. 29–Oct. 3, and approved for publication in the IEEE TRANSACTIONS ON INDUSTRY APPLICATIONS by the Industrial Power Converter Committee of the IEEE Industry Applications Society. This work was supported in part by the European Union's H2020 Research and Innovation programme under Grant 864459 (UE-19-TALENT-864459), in part by the Spanish Government (Innovation Development and Research Office-MEC) under the research grant ENE2016-77919, “Conciliator” Project, and “B2B” Project Nuevas vías hacia la gestión descentralizada de la energía de edificio a edificio PID2019-111051RB-I00, and in part by the Government of the Principality of Asturias, under grant FC-GRUPIN-IDI/2018/000241, and in part by the “Severo Ochoa” Program of Predoctoral Grants for Training in Research and University Teaching under Grant PA-17-PF-BP16-133, and in part by the Instituto de Telecomunicações, Coimbra, Portugal, under Grant UID/EEA/50008/2019.

Sarah Saeed and Jorge Garcia are with the Department of Electrical Engineering, University of Oviedo, 33204 Oviedo, Spain (e-mail: saeedssarah@uniovi.es; garciajorge@uniovi.es).

Marina S. Perdigão is with the Instituto de Telecomunicações, Coimbra, Portugal, and also with the Polytechnic Institute of Coimbra, 3030-199 Coimbra, Portugal (email: perdigao@isec.pt).

Valter S. Costa and André M. S. Mendes are with the Instituto de Telecomunicações, 3030-290 Coimbra, Portugal, and also with the Department of Electrical and Computer Engineering, University of Coimbra, 3030-290 Coimbra, Portugal (e-mail: costinha.96@hotmail.com; amsmendes@deec.uc.pt).

Bruno Baptista is with WEGeuro - Indústria Eléctrica, 4470-605 Maia, Portugal (e-mail: brunobapt@gmail.com).

The magnetic device of interest is the variable inductor (VI). It presents a highly desirable case study, since it is considered a generic case; any model developed for the VI can serve to analyze other nonlinear and multi-winding magnetic devices [1][2]. Moreover, in recent literature, there has been a growing direction to employ the VI in a wide range of applications [3]-[12]. The VI allows for additional degrees of freedom in the design and control of power electronic converters. This is distinctly useful in resonant converters [13], where the usual frequency control has some drawbacks due to Electro-Magnetic Interference (EMI) issues, synchronization, variable sampling time, etc., especially for large range of variation. If variable magnetics are used, the same control margins can be obtained at a constant switching frequency, therefore allowing for an optimization of the EMI filters, and sampling procedures. In other applications such as the Dual Active Bridge (DAB) converter, the variable magnetics can boost the converter efficiency by modifying the operation point to bring the converter operation within the soft switching margins [3][14][15]. Also, the addition of a new degree of freedom to the control allows linearization of the controlled system [3].

In principle, the modeling methods of magnetic devices are confined to either analytical or numerical methods. Specific to VI, modeling strategies are mainly: Finite Element Analysis (FEA) [16][17], gyrator-capacitor model [18][19], and reluctance equivalent circuit [20][21].

FEA models are based on numerical analysis and are considered very powerful to analyze the behavior of magnetic components especially under nonlinear operation. However, they have some drawbacks such as the sensitivity of the solution to geometrical dimensions and material properties, also the amount of data that needs to be post-processed for 3D simulations [22], and moreover, it is not straightforward to move between the magnetic solution and the corresponding electrical circuit model.

Therefore, the methodology followed in this paper is to use the FEA model during the design stage of the magnetic device to acquire the necessary knowledge about the magnetic core behavior under saturation, such as the permeability definition, the flux distribution, and the temperature effect. The effect of those factors can thus be aggregated to the appropriate analytical circuit model. This allows the use of analytical-based models without compromising the accuracy acquired by the FEA-based ones, which enables the use of these accurate models in real-time applications. In this study, the analytical circuit used to model the VI is the reluctance equivalent circuit.

One of the issues of modeling the VI is the inaccuracy of the estimation of the magnitude of inductance variation. This issue arises due to the ill-defined material properties under saturation conditions [23]. The aim of this paper is to set the accurate definitions for the magnetic material properties under saturation operation of the VI magnetic core, such as the permeability, the $B(H)$ curve, and the distribution of saturated regions in the core, which impacts the reluctance path lengths. Therefore, a model is proposed to calculate the accurate inductance value, as well as the magnitude of the inductance variation under different saturation conditions.

In this context, section II explains the reluctance equivalent model corresponding to the studied variable inductor. In section III, the modeling of the device using FEA is presented. Based on the analysis in the latter section, section IV discusses the proposed analytical reluctance model. Section V presents further analysis of the cross-coupling between the core temperature and AC mmf which results in a more accurate prediction of the inductance variation range in the variable inductor as illustrated by the design example in section VI. Finally, section VII summarizes the conclusions of the work.

II. ANALYTICAL MODEL OF VARIABLE INDUCTOR

A. Construction of a Variable Inductor

The main aspects regarding the construction of VIs are strongly related to the selection of the core material since the magnetization curve as well as the hysteresis loop both differ in shape and characteristics with different magnetic materials [9]. While, in terms of core structure, the most popular shapes used are the toroids, and the rectangular-laminated cores (U, E, and I cores). This section reviews the history of the VI device, and henceforth, outlines the VI structures of most relevance in the literature. The designs of most relevance to the application herein can be mainly divided into two: the rectangular cores, and the toroidal cores. The rectangular VI is mainly structured as a double-E [1][9][24][25], a triple-E [26], or a quad-U core [2]. While the toroidal core is composed of two toroids arranged in different configurations in terms of the operating windings [27].

The different rectangular VI configurations are illustrated in Fig. 1a, 1b, and 1c. Moreover, Fig. 1d demonstrates the characteristics of the inductance curve as a function of the DC control current, I_b , for different AC main winding current, I_{ac} . As it can be observed, the inductance value is inversely proportional to the control current. Moreover, the inductance variation range ($L_{max} - L_{min}$) is also inversely proportional to the AC current.

On the other hand, the toroidal configuration is shown in Fig. 2a, while similarly Fig. 2b demonstrates the characteristics of the inductance curve as a function of the DC control current, for different AC main winding current. As it can be observed, the inductance value shows similar characteristics to the rectangular VI configuration under relatively small values of AC current. However, as higher values of I_{ac} are used, the inductance characteristic curve shifts to the right [27]. The initial value of I_{ac} will, thus, dictate in which position is the inductance characteristic curve and, in that sense, by increasing the AC main winding current this curve shifts to the right, whereas decreasing it shifts the curve to the left. This results in two characteristic areas of the inductance curve based on its maximum value: area A (increasing inductance), and area B (decreasing inductance).

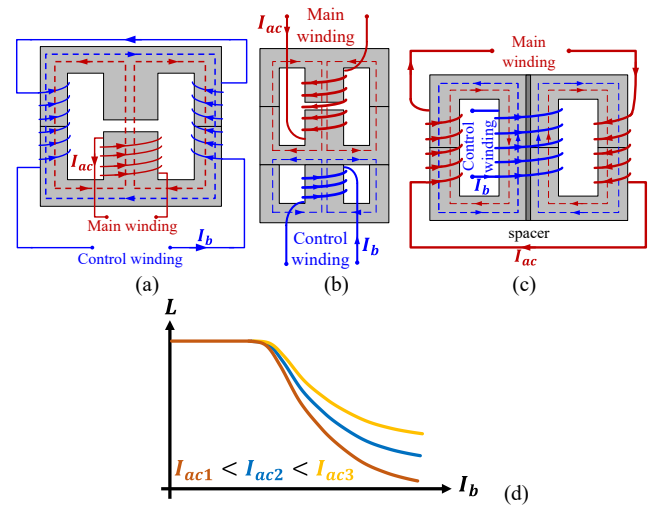


Fig. 1. Different rectangular VI structures and their operation principle. a) Double-E core, b) triple-E core, c) quad-U core, and d) characteristic inductance curve.

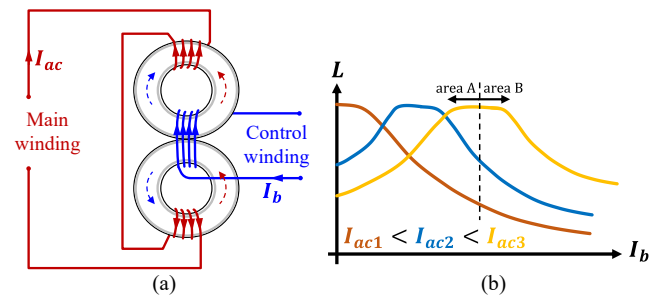


Fig. 2. Toroidal VI structure and its operation principle [27]. a) Configuration, and b) characteristic inductance curve.

The focus of the study herein is on the double E-core VI, therefore, during the following sections, its operation principles will be discussed in detail. The studied concepts, specifically the permeability definition, the inductance computation, and the temperature effect, can be directly applicable to the toroidal cores. However, the study of the distribution of saturated regions in the core, which impacts the reluctance path lengths, is not similar in case of toroidal cores, due to its different magnetic core dimensions.

B. Reluctance Equivalent Circuit

As mentioned before, the reluctance equivalent circuit is used to model the magnetic device under study. Specific to this study, the VI structure used is the double E-core structure [20] depicted in Fig. 3a. Due to the main winding (N_{ac}), an AC flux (ϕ_C) circulates through the center arm and splits to the outer arms. Applying a relatively small DC current (I_b) to the bias control windings (N_b), a DC flux (ϕ_R or ϕ_L) is produced which circulates mainly through the outer (ungapped) circumference of the core [24]. This flux can bias the operation point of the magnetic material towards the nonlinear region, causing the inductance seen from the main winding terminals to vary [20][25]. The operation is clarified by Fig. 3b, which shows the operation points on the $B(H)$ curve for the left and right arms. The constant DC control current will produce a constant mmf in the left and right arms which will bring these sections into the non-linear region of the magnetization curve.

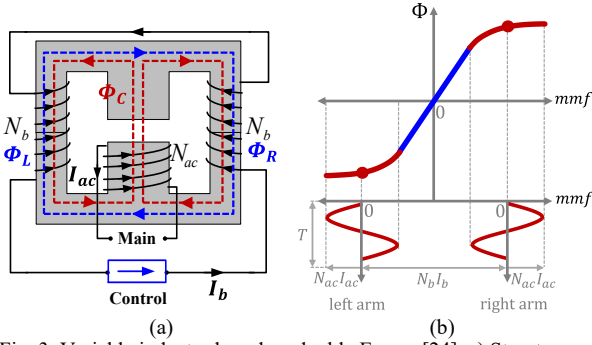


Fig. 3. Variable inductor based on double E-core [24]. a) Structure and windings, and b) principle of operation.

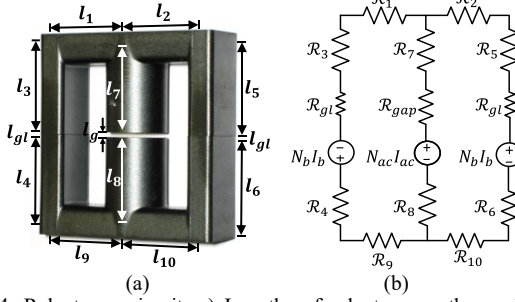


Fig. 4. Reluctance circuit. a) Lengths of reluctance paths, and b) the corresponding circuit model.

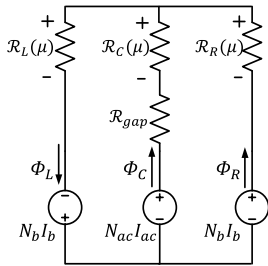


Fig. 5. Reluctance equivalent circuit of the variable inductor in Fig. 1.

The reluctance equivalent circuit is composed of three main elements [20]; a) a constant reluctance which models any non-ferromagnetic material such as air gap, b) a variable reluctance which models the behavior of the ferromagnetic material, and c) a winding model which represents the magnetomotive (mmf) or Ampere-turn of the winding. According to the operation of the device, explained previously, two types of mmf are applied to the device. The AC mmf which is due to main winding current, $N_{ac}I_{ac}$, and the DC mmf which is due to the control current, $N_b I_b$.

Fig. 4a illustrates the lengths of different reluctance paths and Fig. 4b shows the equivalent reluctance circuit model of this magnetic core. The latter circuit can be simplified to the reluctance circuit shown in Fig. 5. The reluctance of a magnetic path is defined by (1).

$$\mathcal{R}_i = \frac{l_i}{\mu_i A_i}, \quad (1)$$

where l_i is the length of the path i , μ_i is the permeability of the magnetic material, and A_i is the cross-sectional area.

C. Magnetic Permeability Definition

The definition of the permeability differs corresponding to the relation between the magnetic flux density, B , and the magnetic field intensity, H , for a certain magnetic material [28], as explained by (2).

$$\mu = B/H \quad (2)$$

However, the permeability has different interpretations depending on the conditions of operation and measurement. A summary of different permeability definitions is provided in [28]. When an AC magnetic field is superimposed on a static or DC magnetic field, a minor hysteresis loop is produced, resulting in the incremental permeability, μ_Δ , defined by (3).

$$\mu_\Delta = \Delta B / \Delta H \quad (3)$$

If the area of the minor loop is relatively small, it reduces to a straight line and therefore, the incremental permeability can be approximated to the differential permeability [29], μ_d , defined by (4). This definition is used in nonlinear and multi-winding systems [30]-[33].

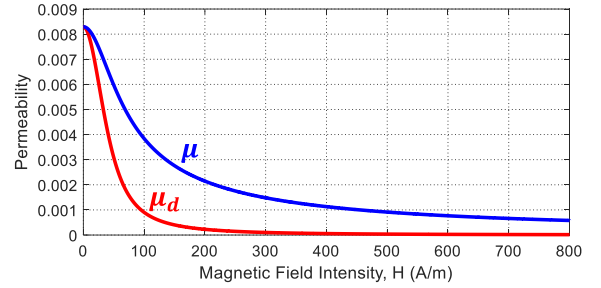


Fig. 6. Permeability definitions for N87 ferromagnetic material.

$$\mu_d(H) = dB(H)/dH \quad (4)$$

The differential permeability, in this context, has been reported to give the most accurate definition of the permeability in nonlinear and multi-winding systems [9] [23]. Therefore, it will be used throughout this study.

Specific to the N87 ferromagnetic material, Fig. 6 compares the permeability, calculated from (2), to the differential permeability, calculated from (4), as a function of magnetic field intensity.

D. Inductance Definition

The inductance can be defined in different ways with respect to the $B(H)$ curve. The first definition, which is also considered as the general definition, states that the inductance, L , is the ratio of the total flux linkage to the current flowing through the winding, as expressed by (5).

$$L = \frac{N_{ac} \Phi_C}{i_{ac}}, \quad (5)$$

where i_{ac} is the AC instantaneous current in the inductor main winding, and Φ_C is the AC flux linking this winding.

The latter definition is satisfactory for a medium with constant permeability, such as air. However, for ferromagnetic materials, a differential inductance is defined, dL , as expressed by (6).

$$dL = \frac{N_{ac} d\Phi_C}{di_{ac}} \quad (6)$$

And finally, considering the reluctance model, the inductance can be calculated based on the reluctances of different paths in the magnetic circuit, as shown by (7).

$$L = \frac{N_{ac}^2}{\mathcal{R}_C(\mu) + \mathcal{R}_{gap} + \mathcal{R}_L(\mu) // \mathcal{R}_R(\mu)}, \quad (7)$$

where $\mathcal{R}_C(\mu)$, $\mathcal{R}_L(\mu)$, and $\mathcal{R}_R(\mu)$ are the reluctances of the center, left and right arms, respectively.

To attain more accuracy in the reluctance equivalent circuit, the fringing effect due to the air gap can be considered [34]. So, the inductance value is corrected by a factor, X_f , which is calculated by (8).

$$X_f = 1 + \frac{l_g}{\sqrt{A_c}} \ln \left(\frac{2h_w}{l_g} \right), \quad (8)$$

where h_w is the total height of the main winding, and A_c is the cross-section area of the center arm. And accordingly, the inductance corrected for fringing, L' , is computed by (9).

$$L' = LX_f \quad (9)$$

Summarizing the previous discussions, it can be concluded that the reluctance, thus, is a function of the permeability, which in turn depends on the $B(H)$ curve of the magnetic material. Operating at the knee or the saturation regions of the $B(H)$ curve, the magnetic material will have completely nonlinear behavior, so the permeability will change as well. Moreover, under different operation points, the $B(H)$ curve of the material changes as a function of the operation temperature of the core. Therefore, the calculation of the permeability, and thus the inductance, becomes a nontrivial task. To attain a deeper understanding of the behavior of the magnetic core under saturation, FEA methodology is used to construct, simulate, and analyze the magnetic device under different operation conditions.

III. MODEL OF VARIABLE INDUCTOR USING FEA

The software package used for FEA simulations is *Altair Flux*TM [35]. Briefly, the FEA simulation is developed in three main steps: first, the construction of the 3D core geometry and the mesh generation. Second, adjusting the physical properties which include defining the materials of the magnetic core and the coils, constructing coil conductors, and assigning different volumes regions. And thirdly, solving the constructed magnetic device under certain scenarios of parameters. The influence of any parameter in a simulation can be explored and visualized through multidimensional curves and animations of color shades or arrows.

A. Construction

The VI was constructed in *Flux*TM 3D, using the dimensions measured by a caliper, to accurately resemble the constructed prototype as it can be observed in Fig. 7. The specifications of the designed VI are stated in Table I.

The *N87* magnetic material $B(H)$ curves, at 25°C and 100°C, were obtained from the manufacturer's datasheet. This was carried out by using a digital image processing tool to accurately extract the numeric data from the $B(H)$ image. The tool used herein is the "Engauge Digitizer" open source software [34]. Then, by using "Interpolation Over a Grid" (*meshgrid* command in *MATLAB*[®]), the $B(H)$ curves at different temperatures were obtained and introduced to the FEA model, as shown in Fig. 8. Linear interpolation was assumed based on the fact that the permeability and the core loss parameters, provided by the magnetic core manufacturer [37], show linear behavior as a function of the temperature for the range between 25°C and 100°C.

Next, the windings' copper material properties were added to the FEA model as well. And finally, the materials were assigned to the corresponding volume regions.

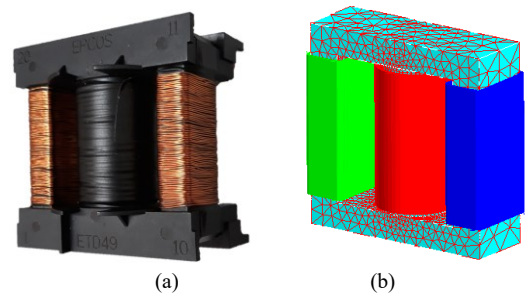


Fig. 7. Variable inductor. a) Prototype based on double E-core, and b) constructed 3D model in *Flux*TM illustrating the meshed magnetic core and the three windings; the main winding in red, and the left and right control windings are in green and blue, respectively.

TABLE I
SPECIFICATIONS OF VARIABLE INDUCTOR PROTOTYPE

Core Size	ETD49/25/16
Magnetic Material	Ferrite N87
ΔL	144 μ H to 50 μ H
N_{ac}	23 turns
N_b	72 turns
l_g	1 mm
Fringing factor, X_f	1.3

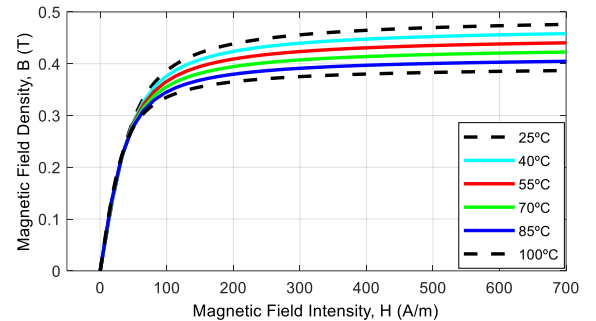


Fig. 8. $B(H)$ curve of *N87* magnetic material for different temperatures.

B. Computing Inductance at Different Bias Currents

In order to study the core under small-signal analysis, the FEA model is adjusted to "Magnetic" application. A scenario was configured to vary the DC current in the control windings from 0 to 1A in steps of 0.1, in order to calculate the inductance value under different bias conditions.

In *Flux*TM, one of the ways to compute the inductance is by using a sensor based on the theoretical definition previously expressed by (5). Also, this simulated inductance is compared to the experimental value obtained from the small-signal measurements using an impedance analyzer model BK Precision 889A Bench LCR/ESR Meter. It is worth to note that during small-signal measurements, the main winding current is relatively small, less than 0.1A, therefore, the current was set in the FEA model to 0.1A to assure accuracy when comparing results.

Fig. 9 shows the inductance as a function of the DC bias current illustrating the FEA simulation results compared to the small-signal experimental measurements. The error between the simulated and measured value is observed to be less than 20%, which is acceptable for this application.

The deviation of the simulation from the experimental results reaches a maximum in the range of 0.2A, this occurs due to disregarding the hysteresis effect in the $B(H)$ curve

since the Flux™ software does not comprise a functionality to account for the hysteresis losses. The latter losses along with the device winding losses have already been analyzed and a full analytical circuit model was proposed for the variable inductor device and implemented on Simulink™ in [36]. The current work is focused on obtaining an accurate estimation of the inductance variation range; therefore, the hysteresis effect was compromised to use the available FEA simulation software. And consequently, the simulation results are carried out to prove that the proposed improvements in the model can lead to better accuracy in estimating the inductance compared to the conventional reluctance circuit model.

This is an opportune point to check the accuracy of the conventional analytical reluctance circuit compared to that of FEA simulation model. Therefore, the inductance is also calculated analytically by computing the reluctances of different magnetic paths, as expressed previously by (7).

To carry out the calculations analytically, the reluctance equivalent circuit is built in the 3D FEA model in order to take advantage of the geometrical dimensions already defined. Therefore, different magnetic paths are drawn in the 3D model by defining discrete 2D lines, as explained by Fig. 10. The permeability is calculated as an average value over each of the paths, as defined by (2). Then, the reluctances of the defined paths are computed.

The resulting inductance curve is thus plotted and compared to the obtained experimental results as shown in Fig. 9. It can be seen that the inductance curve disperses from the experimental measurement especially as the saturation current increases. Therefore, the original equivalent reluctance circuit does not provide enough accuracy under nonlinear operation of the magnetic core material. To understand the limitations to this analytical model, it is necessary to analyze the magnetic core under different saturation conditions.

C. Analysis of Saturation of Magnetic Core

The graphical visualization of the results in the Flux™ 3D software gives more insight to learn about complex quantities such as magnetic flux density, permeability of the magnetic core, field intensity, etc. and their distribution across the core. As an example, Fig. 11 illustrates the 3D core model with the distribution of magnetic flux density at the maximum DC bias current of 1A and very small inductor main current of 0.1A. Different arrows represent the orientation of magnetic flux density, and their colors correspond to the value of magnetic flux density, as explained by the legend at the left of the figure. It can be observed that the values of B are maximum through the outer frame of the core due to the DC bias current which causes a DC flux that saturates this path. Also, it is worth to note that almost no DC flux lines are observed to flow through the center arm, however, they form a closed path around the outer frame of the core. Fig. 11 also demonstrates the different parts of the FEA simulation platform which includes the Graphic window to visualize the 3D core model of the variable inductor illustrating the distribution of the desired operation parameters. Also, the Data Tree window which illustrates the geometry construction and post processing results. Moreover,

the Output window presents the details of the solving process and the results of the nodal analysis.

On the other hand, Fig. 12 shows the differential permeability values graphically represented on the 3D core model in an evolution from no saturation, Fig. 12a, through partial saturation, Fig. 12b, and until maximum saturation, Fig. 12c. Color shading corresponds to the value of magnetic permeability in each zone as explained by the legend at the left of the figure [17].

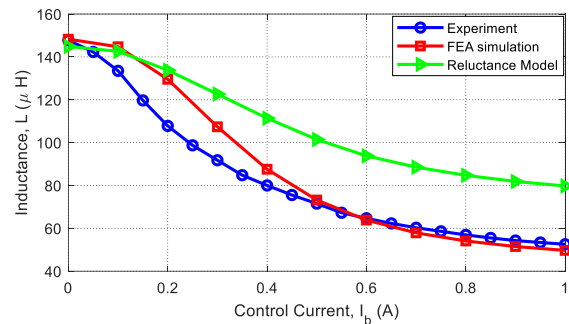


Fig. 9. Inductance as a function of bias control current. FEA computation and original analytical reluctance model compared to the small-signal experimental measurements.

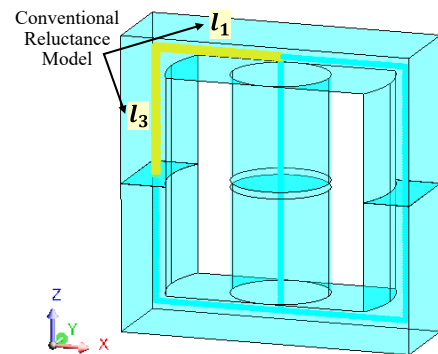


Fig. 10. Constructing different reluctance paths in Flux™ simulation model by defining 2D lines and discretizing the lines to definite number of points.

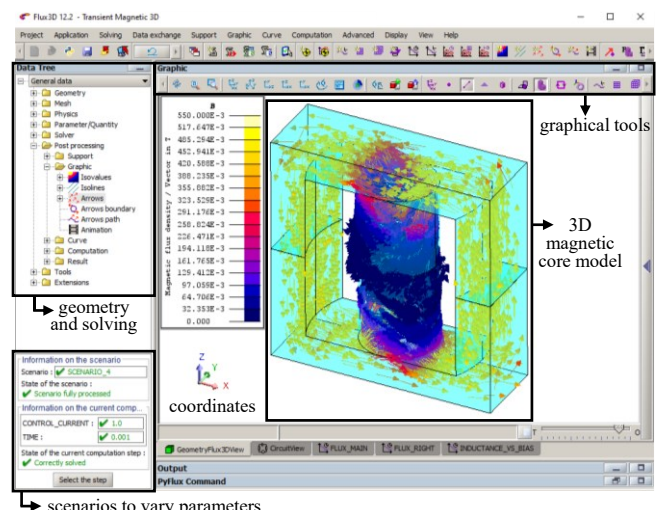


Fig. 11. FEA simulation platform illustrating the results of magnetic flux density distribution visualized on the 3D core model at the maximum DC bias current of 1A.

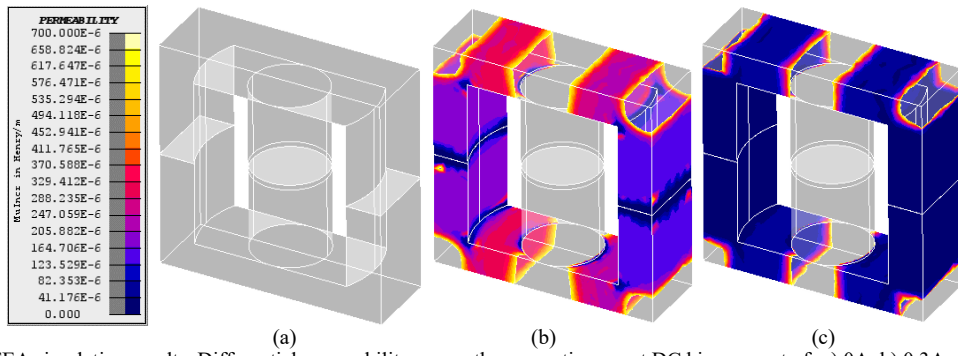


Fig. 12. FEA simulation results. Differential permeability across the magnetic core at DC bias current of: a) 0A, b) 0.3A, and c) 1A.

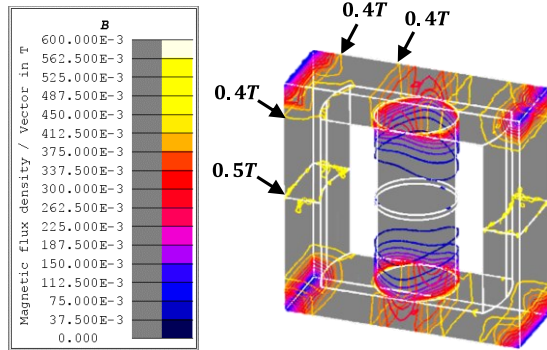


Fig. 13. Contours of magnetic flux density illustrating the boundaries of the saturated regions.

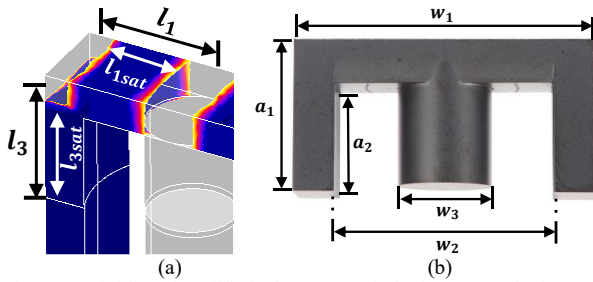


Fig. 14. Definition of modified reluctance paths in the proposed reluctance model. a) Modified lengths, and b) dimensions of the magnetic core.

As it can be seen, the permeability values are nonlinearly distributed across the core and show an evolution of length of saturated paths in the core. Under maximum saturation condition, some parts of the magnetic core, specifically the corner points, are not utilized or in other words unsaturated demonstrating much higher permeability values. Therefore, this issue must be taken into consideration when applying the reluctance circuit to model the magnetic core under saturation. The lengths of different reluctance paths in the magnetic core should be modified according to the saturation condition to correspond to the actual saturated portions of the core [23]. This will be discussed in detail in the following section.

IV. PROPOSED VARIABLE INDUCTOR ANALYTICAL RELUCTANCE MODEL

As it was clarified in the previous sections, the VI device is distinguished by its capability to vary the inductance value. The range of the variation of the inductance depends on the design of the device, however, the design procedure does not guarantee the desired maximum and minimum inductance values. This process is usually iterative and is one of the issues of modeling the VI [23]. The issue arises due to ill-defined material properties under saturation conditions. In this section, a reluctance circuit model is proposed which

provides an accurate estimation of the inductance as a function of the bias control current. The model sets the accurate definitions for the magnetic material properties such as the permeability, the $B(H)$ curve, and the distribution of saturated regions in the core, which impacts the reluctance path lengths.

A. Modification of Reluctance Path Lengths

As it was explained in the previous section, under saturation of the magnetic core, the lengths of different reluctance paths are altered. Specific to the double E-core VI, the saturation takes place mainly in the outer circumference of the core, as explained in section II. Therefore, the lengths of the paths forming this outer frame of the core are modified. As defined by Fig. 4a, l_1 , l_3 , l_4 , and l_9 represent the left magnetic path, while l_2 , l_5 , l_6 , and l_{10} represent the right magnetic path. Due to symmetry, l_1 and l_3 are calculated and applied to the corresponding lengths of the core.

To obtain expressions for the modified lengths, $l_1|_{sat}$ and $l_3|_{sat}$, the contour lines of the magnetic flux density are demonstrated on the 3D model, as shown in Fig. 13. The region of saturation of the N87 magnetic material is between 0.4T to the maximum saturation magnetic flux density of 0.5T, as will be detailed with a design example in section VI. The length of the saturated region, $l_1|_{sat}$ and $l_3|_{sat}$, are bounded by the contour lines, as marked on Fig. 13. Comparing those lengths to the lengths of the full reluctance paths, l_1 and l_3 , as clarified by Fig. 14a, and by using curve fitting an expression is obtained for the length of the saturated region as a function of the magnetic core dimensions defined by Fig. 14b.

Consequently, equations (10) and (11) state the calculation of the modified lengths of those reluctance paths under saturation.

$$l_1|_{sat} = \frac{w_3}{16} + \frac{w_2 - w_3}{2} + \frac{w_1 - w_2}{8} \quad (10)$$

$$l_3|_{sat} = a_2 + \frac{a_1 - a_2}{4} \quad (11)$$

The initial approach to obtain those equations are based on experimental observations during several tests carried out on E-core variable inductors and first presented in [23]. In this latter literature work, the equations were verified for the magnetic core sizes: ETD49, EFD25 and EF25, as well as for different values of air gaps. Therefore, the equations are considered accurate for E-shaped VI cores.

The modified reluctance path lengths are then substituted in (1) along with the value of the differential permeability, defined by (4), to calculate the reluctances of different magnetic paths. Consequently, to compute the inductance, the reluctance values are substituted in (7).

B. Error Analysis of the Modified Lengths

By applying the previously detailed calculations, Fig. 15a shows the inductance as a function of the control current. The plot illustrates the results of the proposed model and the original reluctance circuit model both compared to the experimental results. The inductance value obtained from the proposed reluctance model is observed to give more accuracy compared to the original reluctance circuit model especially as the saturation current increases. To further clarify the results, the error calculated for each of the models compared to the experimental measurements is illustrated in Fig. 15b. As it can be observed, at low bias currents, both the original and the proposed models show a similar error. However, as the saturation current increases the proposed model shows a reduced error, in comparison with the original reluctance model whose error reaches around 60% at the maximum bias current of 1A, which is almost three times the error achieved by the proposed model.

The original reluctance circuit model has been used as the conventional approach to study the behavior of the magnetic core [20][39]. However, the applicability of the model is mostly limited to the linear region of operation of the magnetic core material within the $B(H)$ curve. Under deep saturation of the magnetic material, the original reluctance model fails to provide an accurate estimation of the inductance value [1][23], as observed from the previous analysis. Therefore, the use of differential permeability and the modified reluctance path lengths, included in the proposed model, is essential to predict the inductance variation with more accuracy.

It is worth to note that the similar error observed in both the original and the proposed models when compared to the experimental results is due to disregarding the hysteresis effect. As mentioned previously, the accuracy of the models is jeopardized by the limited functionalities of the available FEA simulation software. Modeling the device including core and winding losses has been the focus of a previous work [25][38]. However, for a comparative point of view, Fig. 16 illustrates the inductance curve predicted by the proposed model when adding the device losses to the reluctance equivalent circuit. The losses considered are mainly the winding losses (calculated by Dowell's equations [40]) and the hysteresis losses (calculated by Jiles-Atherton equations [16]).

It can be observed from Fig. 16b that the error of the proposed model compared to the experimental results, around 0.2A control current, has a maximum of 8%, which is improved from 28% observed in Fig. 15b when disregarding the hysteresis losses. Also, as the control current increases, the error in case of considering the hysteresis losses tends to decrease to reach approximately 0.5% at the maximum saturation level.

C. Impact of Core Temperature on the Inductance

From the above discussions, it can be concluded that the inductance value depends on the operation point of the magnetic material on the $B(H)$ curve. The $B(H)$ curve of the material can vary depending on the temperature of operation as well. There are no previous studies which considered the effect of temperature dependence of $B(H)$ curve on the inductance calculation in variable inductors. Specific to those devices, the temperature of

the core can have a significant effect on the range of variation of the inductance, which in the end impacts the design of the device.

In this work, some experimental measurements are carried out to understand the temperature effect on the inductance variation range, and eventually include this effect in the full design process of the VI. Fig. 17 shows a circuit diagram of the test platform used for the experiments. An H-bridge is constructed to apply an AC square waveform excitation voltage to the inductor main winding. A DC current is applied to the inductor control windings which is obtained by a DC voltage supply connected in series with a resistance to have a maximum of 1A.

The test setup is illustrated in Fig. 18, and the design specifications are listed in Table II. Three tests have been carried out at three different DC-link input voltages: $V_{in} = 10V$, 30V, and 50V. At each operation condition, the inductance value is varied from maximum to minimum values by means of varying the control current from 0 to 1A. Fig. 19 shows the waveform of the main winding current, $i_{ac}(t)$, for the three operation conditions at 1A control current.

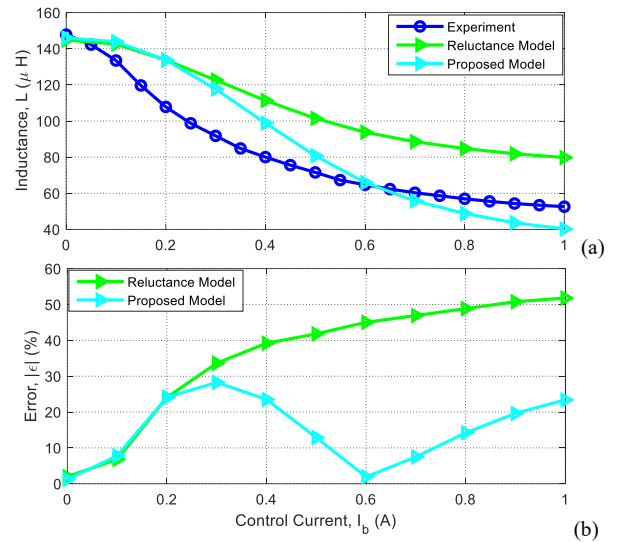


Fig. 15. Inductance calculation. Proposed analytical reluctance model versus original reluctance equivalent circuit compared against experimental measurements. a) Inductance, and b) magnitude of error, as a function of the bias control current.

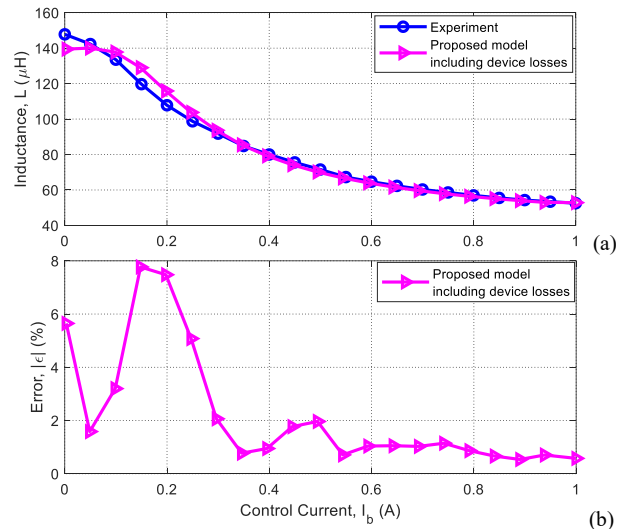


Fig. 16. Inductance calculation. Proposed analytical reluctance model including device losses compared to the experimental measurements. a) Inductance, and b) magnitude of error, as a function of the bias control current.

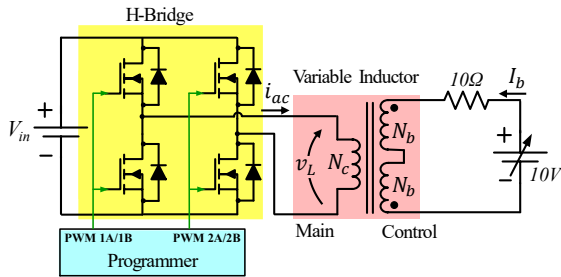


Fig. 17. Circuit diagram of the test platform.

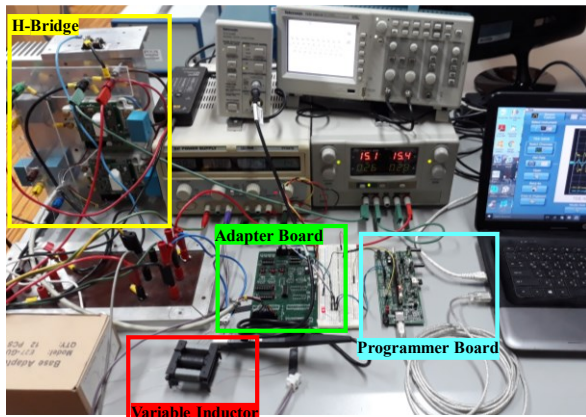


Fig. 18. Experimental test setup.

TABLE II
SPECIFICATIONS OF TEST SETUP

H-bridge	
IGBT module	SEMiX202GB066HDS
Adapter board	Board 2S SKYPER 32 PRO
Driver core	SKYPER 32 PRO
Programmer	
DSP board	TMS320F28335 controlCARD
Variable Inductor	
Core size	ETD49/25/16
Magnetic material	Ferrite N87
Inductance variation range, ΔL	144 μ H to 50 μ H
Operation Conditions	
Input voltage, V_{in}	0 – 50V
Switching frequency, f	20kHz
Inductor peak current	10A
Temperature	25°C – 70°C

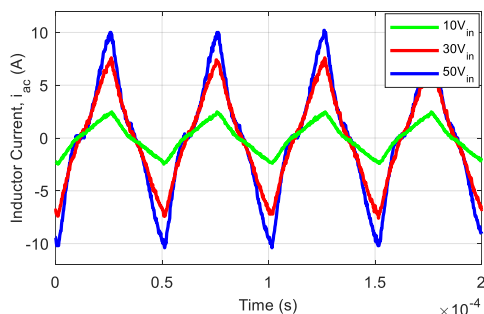


Fig. 19. Inductor current waveform at 1A control current for three different operation conditions at DC-Link input voltage of 10V, 30V, and 50V.

The inductance value is calculated using the RMS values of the first harmonic component of the voltage and current measurements, so the resulting inductance is calculated by (12).

$$L = \frac{X_L}{\omega} = \frac{V_L}{I_{ac}} \cdot \frac{\pi/4}{2\pi f}, \quad (12)$$

where V_L is the RMS value of the voltage measured across the main winding of the VI, and I_{ac} is the RMS value of current flowing through this winding.

It is worth to note that using the fundamental components simplifies the calculation of the inductance without compromising the accuracy of the measured value. This conclusion was based on comparing the results obtained by using this method to those obtained by using instantaneous measured waveforms applied to *System Identification Tool* from MATLAB[®]. The inductance values calculated showed a very close agreement which justifies the simplification [39].

Fig. 20a illustrates the inductance curves as a function of the control current for each power level. The inductance variation range is calculated by (13).

$$\Delta L = (L_{max})_{I_b=0} - (L_{min})_{I_b=1} \quad (13)$$

It can be observed that as the power level increases, from 10V_{in} to 50V_{in}, the inductance variation range is reduced from 93 μ H (144-51 μ H) to 70 μ H (144-74 μ H), which is around 16% reduction.

The temperature was recorded during each test using FLIR[®] thermal camera. Taking into consideration the time the magnetic core temperature reaches steady state, at each test the core is left around 15 minutes to settle down before taking the temperature measurement.

Fig. 20b illustrates the temperature curves as a function of the control current for each power level. The temperature gradient is calculated by (14).

$$\Delta T = (T_{max})_{I_b=1} - (T_{min})_{I_b=0} \quad (14)$$

It can be observed that as the power level increases, from 10V_{in} to 50V_{in}, the temperature gradient is increased from 11.6°C (38.6-27°C) to 28.2°C (65.9-37.7°C). The temperature gradient, ΔT , is plotted against the corresponding inductance variation range, ΔL , as shown in Fig. 21, which demonstrates that the inductance variation range is inversely proportional to the temperature gradient, as clarified by (15).

$$\Delta L \propto \frac{1}{\Delta T} \quad (15)$$

It has been concluded from the experiments that there is a cross-coupling between the temperature effect and the value of the AC inductor current flowing through the main winding. Therefore, the variation range of the inductance, is not only affected by the temperature of operation of the core, but also by the *mmf* of the main winding. A knowledge of the relationship between the inductance value, temperature of operation, and the inductor currents is, therefore, essential to estimate an accurate value of the inductance under saturation conditions particularly at higher power levels of inductor operation. This is presented in detail in the following section.

V. CROSS-COUPLING BETWEEN TEMPERATURE AND MMF

From the experiments illustrated in Fig. 20, it can be concluded that increasing the power level of operation, i.e. increasing AC *mmf*, will result in an increase in the

temperature gradient of the magnetic core. This temperature increase affects the $B(H)$ curve of the magnetic core, as it is previously illustrated by Fig. 8, with the increase of T , B_{max} decreases. This will result in a reduced permeability and, consequently, a higher reluctance value which will result in a lower inductance value, as it can be observed from the experimental inductance curves in Fig. 20a.

However, besides the temperature effect, the AC mmf level in itself affects the inductance value, especially under nonlinear operation of the magnetic core. This takes place because the change in the AC mmf will result in a change in the AC flux in the center arm of the core. Since the inductance value is defined as the ratio of the flux linkage to the current, thus the variation of the AC flux will directly affect the value of the inductance measured from the winding across this arm (main winding), as previously explained by Fig. 3b.

As it has been clarified previously, there is a cross-coupling between the effects of the core temperature and the AC mmf on the value of the inductance. Therefore, there is no direct relationship that can describe the inductance variation as a function of the core temperature nor the AC mmf separately. The solution is to decouple the effects of both factors, and to generate a 3D lookup table/map to explain the inductance as function of, not only the DC control current, but also AC mmf , and reproduce this map for different core temperatures. To this motivation, FEA simulations were carried out to study the effect of each factor alone.

A. Decoupling the mmf and the Core Temperature Effects on the Inductance Computation

During the first simulation, the AC mmf is kept constant while the core temperature is increased from 25°C to 100°C, by configuring the corresponding $B(H)$ curve of the magnetic material at these temperature values. The inductance is thus computed as a function of the bias control current, Fig. 22a. It can be observed from the plot that the inductance curves shift down as the core temperature is increased. During the second simulation, the core temperature is kept constant at 25°C, while the AC mmf is changed, by varying I_{ac} . Fig. 22b shows the inductance curves as a function of the bias control current. It can be observed that the inductance value increases as I_{ac} is increased from 1A to 6A.

Combining the curves in Fig. 22, the inductance value can be represented as a function of the control current as well as the main winding RMS current for different temperature values, 25°C and 100°C, as it can be seen in Fig. 23.

Two observations can be made from this figure; first, it can be seen that going from 25°C to 100°C temperature, the values of $L(I_b, I_{ac})$ is decreased almost in a linear manner (curve translated downwards as clarified by arrow 1), and second, as I_b increases from 0 to 1A, the effect of I_{ac} on the inductance becomes more significant as it is clarified by arrow 2. The arrow shows that the inductance value at $I_b=1A$ is increases as a function of I_{ac} . This change in the inductance value can be accounted for at the design stage of the variable inductance.

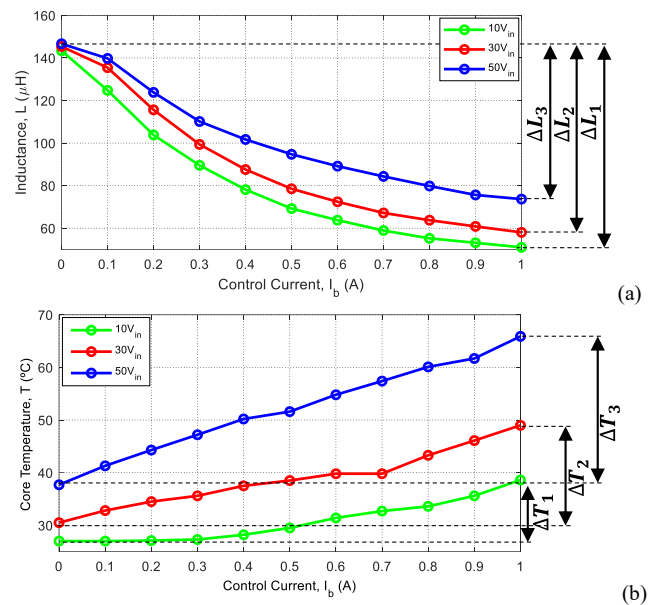


Fig. 20. Temperature effect on inductance value. a) measured inductance, and b) corresponding temperature as a function of bias current.

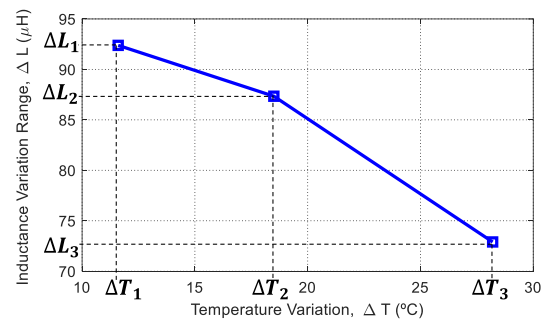


Fig. 21. Inductance variation range as a function of temperature gradient.

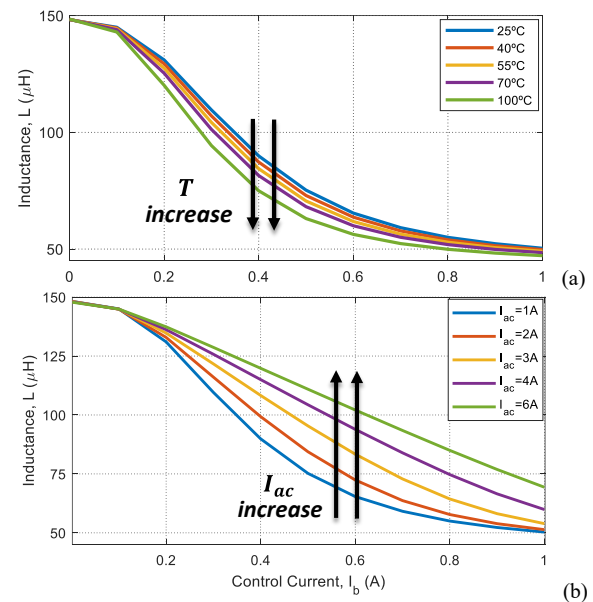


Fig. 22. FEA simulations. Inductance as a function of the bias control current, at: a) different core temperatures, and b) different AC RMS currents.

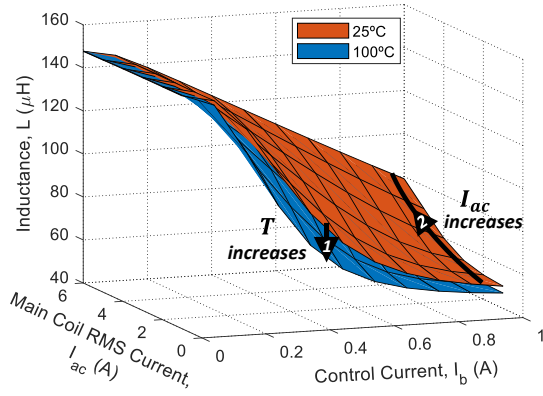


Fig. 23. 3D plot of inductance as a function of control current, I_b , and main current, I_{ac} , for different value of core temperature.

The objective of this study is to provide an accurate estimation of the inductance variation range, $\Delta L = L_{max} - L_{min}$. The maximum inductance (at $I_b = 0A$) does not show any change in terms of temperature nor AC current. On the other hand, the minimum inductance (at $I_b = 1A$) shows a relatively small change as a function of the temperature, but a significant change as a function of the AC current. Therefore, it can be understood that ΔL changes due to the change of L_{min} since L_{max} is constant. To further clarify this, Fig. 24 illustrates ΔL as a function of I_{ac} for different values of temperature based on the FEA simulation results presented previously in Fig. 22 and Fig. 23.

As conceived from the previous discussion, due to any change in the magnetic core temperature or the AC mmf , the L_{min} predicted by the design of the VI will be different from the experimental value. Using the FEA analysis carried out previously, the L_{min} predicted by the design can be corrected on a basis of multiplying the L_{max} by a correction factor. This factor is a function of the temperature as well as the AC mmf . For this reason, it is essential to define the inductance range ratio, r_a [23]. It is the ratio between the maximum and the minimum inductance, as explained by (16).

$$r_a = \frac{L_{max}}{L_{min}} \quad (16)$$

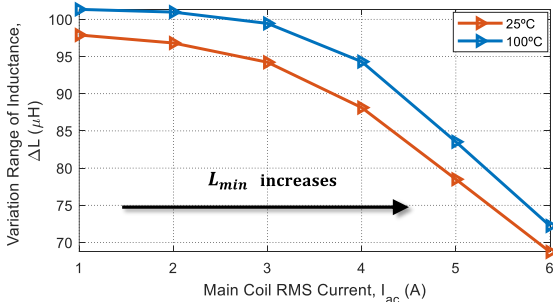


Fig. 24. Inductance variation range, $\Delta L = L_{max} - L_{min}$.

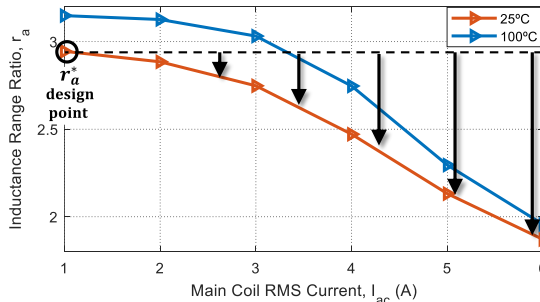


Fig. 25. Inductance range ratio, $r_a = L_{max}/L_{min}$.

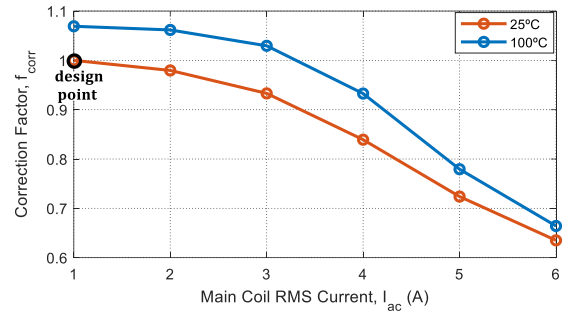


Fig. 26. Correction factor for the design of variable inductor.

Accordingly, L_{min} is calculated by multiplying L_{max} by the factor $1/r_a$. Therefore, if r_a could be computed as a function of the temperature and the AC mmf , the corrected L_{min} could be obtained.

Based on the FEA simulation results, r_a can be calculated as previously explained by (16) for each I_{ac} value and repeating the calculation for different temperature values. The obtained r_a curves, for 25°C and 100°C, are demonstrated in Fig. 25. The point $I_{ac} = 1A$ is considered to be the initial point at which the AC mmf has no effect on the inductance. Thereby, the value of r_a at 25°C is considered the design point, i.e. the point provided by the analytical calculations. It can be seen marked on the figure by r_a^* . This will be clarified in detail with a design example in the following section. Moreover, observing the curves, it can be seen that as I_{ac} increases, r_a decreases from the design point, as demonstrated by the arrows.

To generalize the study for any required design values, the curves are divided by r_a^* . Therefore, a normalized factor, f_{corr} is obtained, which is defined by (17).

$$f_{corr} = \frac{r_a}{r_a^*} \quad (17)$$

Fig. 26 illustrates the curves for f_{corr} as function of I_{ac} for two different temperature values. As it can be observed, the value of the correction factor is 1 at the design point, at 25°C, and decreases below 1 for different values of I_{ac} . Correspondingly, the corrected L_{min} is calculated by (18).

$$L_{min} = L_{max} \cdot \frac{1}{r_a^* \cdot f_{corr}} \quad (18)$$

The physical interpretation of the previous discussion is that the value of L_{min} that the VI can provide, in practice, will depend in a major way on the value of I_{ac} at which the inductor will operate, but also in a minor way on the temperature of operation of the magnetic core. More explicitly explained; as the I_{ac} increases, the value of L_{min} that the VI can provide is expected to be higher, while on the other hand, as $T^\circ C$ increases, of L_{min} that the VI can provide is expected to be lower.

Also, it is worth to note that, once the FEA simulation results have been obtained and the 3D graph values are recorded as a 3D lookup table, the corrected L_{min} could be calculated for any required design based on the same magnetic material and core geometry, i.e. N87 magnetic core based on ETD49/25/16.

B. Empirical Estimation of Core Temperature Rise due to Device Losses

The temperature rise of the magnetic core can be estimated analytically by several means, the simplest is by using the

empirical formulas provided by some core manufacturers [41][42], the most common of which is explained by (19).

$$\Delta T = \left(\frac{P_t}{A_s} \right)^{0.833}, \quad (19)$$

where ΔT is the temperature rise in $^{\circ}\text{C}$, P_t is the total power losses in the magnetic device in mW, and A_s is the surface area of the magnetic core in cm^2 .

The total power loss of the magnetic device is composed of two main components: the winding losses and the core losses.

To compute the winding losses, the DC and AC resistances of each winding are obtained using the Dowell model equations [40], as explained in detail in [43]. On the other hand, to compute the core losses, an empirical formula is used which is known as the Improved Generalized Steinmetz Equation (iGSE) [44-46].

By computing the total power losses in the variable inductor device, a theoretical estimation of the magnetic core temperature rise could be computed. To validate this theoretical estimation, it is worth comparing the empirical temperature rise against the measured one. For this purpose, the experimental results at $50V_{in}$ are captured and used to compute the device losses and estimate the core temperature rise.

Table III illustrates the results of the core temperature estimation at three points of operation of the DC bias current, compared to the corresponding measured values. Comparing the estimated core temperature values to the measured ones for the three points, it can be observed that the empirical estimation presents enough accuracy, where the maximum recorded error between both values does not exceed 5%.

TABLE III
EMPIRICAL ESTIMATION OF CORE TEMPERATURE RISE

I_b	P_t	Estimated T	Measured T	$ e $
0A	1.2779W	37.2039 $^{\circ}\text{C}$	37.7 $^{\circ}\text{C}$	1.3%
0.5A	2.3928W	49.0102 $^{\circ}\text{C}$	51.6 $^{\circ}\text{C}$	5%
1A	4.2523W	66.834 $^{\circ}\text{C}$	65.9 $^{\circ}\text{C}$	1.4%

VI. DESIGN EXAMPLE OF VARIABLE INDUCTOR

As an application example, the VI is designed to replace the constant inductance in a DAB converter [3]. The design values obtained hereafter are the same for the VI prototype used during the experiments. In this manner the corrected inductance values, at different AC mmf values and different core temperature, can be compared against the obtained experimental results.

Henceforth, the following are some simple steps to follow for an accurate design of the VI.

- *Select core material:* this depends on the desired magnetization properties and saturation point. Ferrite N87 is selected as a soft magnetic material for this application. The material properties at 25°C are: $H_{max}=1200\text{A/m}$, and $B_{max}=0.5\text{T}$.
- *Select core shape and size:* the core shape selected is the double E-core structure which provides the symmetrical operation required for the DAB converter. Also, the magnetic core size is selected based on the power level of operation of the core. For this application, a 2kW power

level is sought, thereby ETD49/25/16 core is selected [23]. The corresponding reluctance path lengths and specifications of the core are stated in Table IV.

- *Calculate the number of turns of inductor windings:* the number of turns of the main winding is selected based on the maximum amount of AC field intensity that will be applied to the core, H_{AC} , as calculated by (20).

$$H_{AC} = \frac{N_{ac} I_{ac}}{l_c}, N_{ac} = \frac{H_{AC}(l_7+l_8)}{I_{ac}} = \frac{400 \cdot 219e^{-3}}{5} \approx 23 \text{ turns} \quad (20)$$

On the other hand, the number of turns of the control winding is selected based on the maximum amount of DC field intensity that will be applied to the core, H_{DC} , as calculated by (21).

$$H_{DC} = \frac{N_b I_b}{l_R}, N_b = \frac{H_{DC}(l_1+l_3+l_4+l_9)}{I_b} = \frac{800 \cdot 88e^{-3}}{1} \approx 72 \text{ turns} \quad (21)$$

The H_{DC} field is calculated based on the magnetic material $B(H)$ curve to guarantee the operation in the knee or the saturation regions [20][25].

Another approach to select the number of turns of the control winding is minimizing the magnetic device losses, specifically the winding losses. As the number of turns of the control winding increases, the slope of variation of the inductance as a function of the control current could be increased and, consequently, allowing for a decrease of the control current which would reduce the losses in the winding. However, increasing the number of turns would also implicate an increase in the induced voltage in the control windings. Moreover, this induced voltage is not fully cancelled by the opposite polarity of the left and right control windings, as it can be seen by observing the color differences between the left and right control arms in Fig. 12b. Therefore, for some applications, a high level of induced voltage would mean jeopardizing the safety or imply modifying the system design to handle those voltages. For example, in LED drivers, the level of the induced voltage would affect the light quality [26]. On the other hand, in applications such as electric vehicles, an increased induced voltage could be acceptable on the cost of reducing the volume of the full system [47]. Consequently, there is not a straightforward procedure to select the number of turns of the variable inductor, however, the design depends to a great extent on the application requirements.

- *Calculate the differential permeability:* it is calculated by getting the derivative of B with respect to H , as clarified previously by (4). The $B(H)$ curve can be extracted from the datasheet or calculated by means of Brauer's model or Jiles-Atherton (JA) model [25]. The differential permeability at no saturation for N87 magnetic material is given by $\mu_0 \mu_d = 8.4e^{-3}$, while the value at maximum saturation is given by $\mu_0 \mu_{dsat} = 5e^{-5}$, which can be extracted from Fig. 6.
- *Calculate the inductance maximum and minimum values:* those values are calculated by using equations (22) and (23). The reluctances of different magnetic paths are calculated by substituting the corresponding path length, Fig. 4, and permeability of the material into (1). Table V summarizes the calculated values for the reluctances of different paths.

$$L_{max} = \frac{N_{ac}^2}{\mathcal{R}_g + 2\mathcal{R}_7 + \mathcal{R}_1 + \mathcal{R}_3} \approx 144 \mu\text{H} \quad (22)$$

$$L_{min} = \frac{N_{ac}^2}{\mathcal{R}_g + 2\mathcal{R}_7 + \mathcal{R}_{1sat} + \mathcal{R}_{3sat}} \approx 50 \mu\text{H} \quad (23)$$

The ratio factor, r_a , is the ratio between the maximum and minimum inductances, and can be calculated by (24).

$$\begin{aligned} r_a^* &= \frac{L_{max}}{L_{min}} = \frac{N_{ac}^2 / (\mathcal{R}_g + 2\mathcal{R}_7 + \mathcal{R}_1 + \mathcal{R}_3)}{N_{ac}^2 / (\mathcal{R}_g + 2\mathcal{R}_7 + \mathcal{R}_{1sat} + \mathcal{R}_{3sat})} \\ &= \frac{\left(\frac{l_g}{\mu_0 A_c} + 2 \frac{l_7}{\mu_0 \mu_d A_c} + \frac{l_{1sat}}{\mu_0 \mu_{dsat} A_b} + \frac{l_{3sat}}{\mu_0 \mu_{dsat} A_b} \right)}{\left(\frac{l_g}{\mu_0 A_c} + 2 \frac{l_7}{\mu_0 \mu_d A_c} + \frac{l_1}{\mu_0 \mu_d A_b} + \frac{l_3}{\mu_0 \mu_d A_b} \right)} \\ &\approx 2.9 \end{aligned} \quad (24)$$

- **Obtain the 3D lookup table and the correction factor using FEA simulations:** the FEA model, previously explained in section III, is simulated to get the values of the inductance as a function of I_{ac} and $T^\circ C$. The data is then represented in a 3D lookup table/map. The data for this example is for ETD49/25/16 core based on N87 magnetic material which has already been obtained and illustrated in Fig. 23. Using the obtained data, the correction factor can be computed by (16) and (17).
- **Calculate the corrected minimum inductance:** the corrected L_{min} is computed by multiplying L_{max} by the correction factor, as expressed previously by (18).

To be able to compare the corrected values with the measured ones obtained through the experimental results, the L_{min} is calculated for the same values of I_{ac} and $T^\circ C$ measured through the tests. Going back to Fig. 19 and Fig. 20, it is recalled that three tests were carried out: at 10V_{in}, 30V_{in}, and 50V_{in}. The values of I_{ac} for the three experiments are calculated by taking the RMS of the current curves $i_{ac}(t)$ at the maximum DC control current of 1A, which are shown in Fig. 19. The resulting values are summarized in Table VI. Similarly, the temperature of the core is measured from Fig. 20b at the maximum DC control current of 1A, and the values corresponding to the three experiments are summarized in Table VI as well.

TABLE IV
DIMENSIONS OF THE SELECTED CORE

Lengths of reluctance paths of lateral arms	$l_1 = l_2 = l_9 = l_{10}$	21.5mm
	$l_3 = l_4 = l_5 = l_6$	21.44mm
Lengths of reluctance paths of center arms	$L_7 = L_8$	20.95mm
Modified lengths	l_{1sat}	15.8mm
	l_{3sat}	19.8mm
Cross section area of center arm	A_c	207.39mm ²
Cross section area of lateral arms	A_b	105.56mm ²

TABLE V
RELUCTANCES OF MAGNETIC PATHS

Reluctance of air gap	\mathcal{R}_g	$\frac{l_g}{\mu_0 A_c} = \frac{1e^{-3}}{4\pi * 10^{-7} * 207.39e^{-6}} = 3.837e^6 \Omega$
Reluctance of l_7 path	\mathcal{R}_7	$\frac{l_7}{\mu_0 \mu_d A_c} = \frac{20.95e^{-3}}{8.4e^{-3} * 207.39e^{-6}} = 1.2026e^4 \Omega$
Reluctance of l_1 path	\mathcal{R}_1	$\frac{l_1}{\mu_0 \mu_d A_b} = \frac{21.5e^{-3}}{8.4e^{-3} * 105.56e^{-6}} = 2.4247e^4 \Omega$
	\mathcal{R}_{1sat}	$\frac{l_{1sat}}{\mu_0 \mu_{dsat} A_b} = \frac{15.8e^{-3}}{5e^{-5} * 105.56e^{-6}} = 2.9936e^4 \Omega$
Reluctance of l_3 path	\mathcal{R}_3	$\frac{l_3}{\mu_0 \mu_d A_b} = \frac{21.44e^{-3}}{8.4e^{-3} * 105.56e^{-6}} = 2.4179e^4 \Omega$
	\mathcal{R}_{3sat}	$\frac{l_{3sat}}{\mu_0 \mu_{dsat} A_b} = \frac{19.8e^{-3}}{5e^{-5} * 105.56e^{-6}} = 3.7514e^4 \Omega$

Based on the values of I_{ac} and $T^\circ C$, the corresponding correction factor is extracted from Fig. 26. Using linear interpolation, f_{corr} values at any current or temperature can be obtained. For more clarification, the correction factor values corresponding to those three points are marked on Fig. 27.

To have a visual comparison, the corrected L_{min} values stated in Table VI are illustrated in Fig. 28 along with the corresponding experimental values of the minimum inductance extracted from Fig. 20a at the maximum DC control current of 1A. Also, the design value, calculated by (23) to be 50μH, is included in the figure for comparison.

It can be observed from Fig. 28a that the design value does not correctly predict the inductance, since the experimental inductance values increase as I_{ac} increases. While, on the other hand, using the correction factor proposed, the corrected inductance values match the experimental value with an increased accuracy as I_{ac} increases. The same conclusion can be conceived from Fig. 28b, where the inductance value is illustrated as a function of the core temperature, T .

TABLE VI
CALCULATION OF CORRECTED MINIMUM INDUCTANCE

I_{ac}	T	f_{corr}	Corrected L_{min}
1.4A	40°C	0.99	$\frac{L_{max}}{r_a^* \cdot f_{corr}} = \frac{144}{2.9 * 0.99} = 50.16\mu H$
4.3A	50°C	0.86	$\frac{L_{max}}{r_a^* \cdot f_{corr}} = \frac{144}{2.9 * 0.86} = 57.74\mu H$
5.8A	70°C	0.68	$\frac{L_{max}}{r_a^* \cdot f_{corr}} = \frac{144}{2.9 * 0.68} = 73.02\mu H$

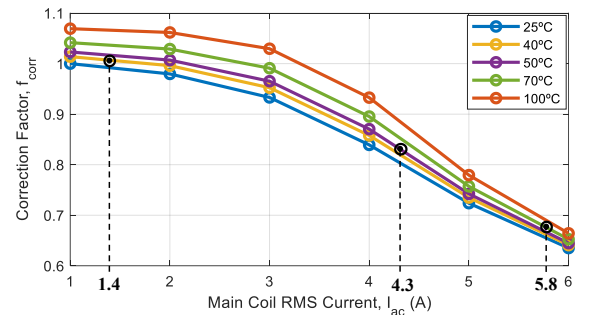


Fig. 27. Correction factor curves as a function of the AC RMS current for different values of core temperature. The plot illustrates the three points at which the corrected L_{min} is calculated.

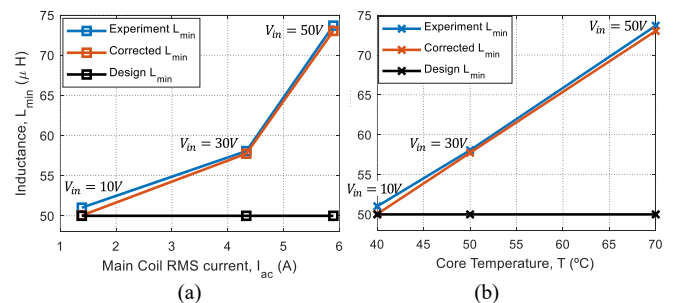


Fig. 28. Corrected inductance value at 1A bias current compared to experimental measurements illustrated as a function of: a) the AC RMS current, I_{ac} , and b) the core temperature, T .

VII. CONCLUSIONS

The paper presented a study of the inductance calculation in variable inductor. A modified analytical reluctance model has been proposed, which gives better accuracy to the inductance calculation especially under saturation of the magnetic core. The contributions of the proposed model compared to the conventional reluctance equivalent circuit consist in three main points. First, the permeability is redefined to use the differential permeability for describing the nonlinear behavior of the magnetic material. Second, through simulations of the device using FEA more insight was given to the permeability distribution in the magnetic core under saturation. Based on these simulations, the reluctance path lengths were modified to exclude unutilized partitions of the core. Thirdly, the temperature dependence of the magnetic material has been explored through FEA simulations as well as experimental measurements to study its effect on the inductance variation range. Additionally, an analytical approach to estimate the core temperature rise as a function of the device power losses has been elaborated and validated in comparison to the experimental results.

Understanding the cross-coupling between the core temperature and the AC mmf resulted in an improvement in the design of the inductor to predict a more accurate inductance variation range specifically under high AC currents. Moreover, a procedure was constructed to compute a correction factor for an accurate estimation of the inductance variation range in terms of the operation parameters; mainly the AC mmf and the core temperature. Furthermore, the obtained factor is normalized to allow the use of the data for any design of a variable inductor based on the same magnetic material and geometry, i.e. N87 material and ETD49/25/16 core.

The proposed analytical reluctance model, therefore, has a compared accuracy to that of the FEA-based model. The adjustments proposed in this paper allow to bridge the gap between the accuracy provided by the FEA simulations and that of analytical solutions in describing the nonlinear behavior of the variable inductor.

As a future development, the proposed modification of the reluctance path lengths could be applied to study the quad-U core VI structure to prove that excluding the corner points of the rectangular cores would save unused magnetic material.

REFERENCES

- [1] S. Saeed, J. Garcia, M. S. Perdigão, V. S. Costa, B. Baptista and A. M. S. Mendes, "Improved inductance calculation in variable power inductors by adjustment of the reluctance model through magnetic path analysis," 2019 IEEE Energy Conversion Congress and Exposition (ECCE), Baltimore, MD, USA, 2019, pp. 6634-6640.
- [2] J. M. Alonso, M. Perdigão, M. A. Dalla Costa, S. Zhang and Y. Wang, "Analysis and experimentation of the quad-U variable inductor for power electronics applications," in *IET Power Electronics*, vol. 11, no. 14, pp. 2330-2337, 27 11 2018, doi: 10.1049/iet-pel.2018.5126.
- [3] S. Saeed and J. Garcia, "Extended Operational Range of Dual-Active-Bridge Converters by using Variable Magnetic Devices," 2019 IEEE Applied Power Electronics Conference and Exposition (APEC), Anaheim, CA, USA, 2019, pp. 1629-1634.
- [4] A. A. Huzayyin, "Utilizing the nonlinearity of a magnetic core inductor as a source of variable reactive power compensation in electric power systems," in Proc. Annu. IEEE Conf. Student Paper, 2008, pp. 1-4.
- [5] S. Aldaher, P. C.-K. Luk, and J. F. Whidborne, "Electronic tuning of misaligned coils in wireless power transfer systems," *IEEE Trans. Power Electron.*, vol. 29, no. 11, pp. 5975-5982, Nov. 2014.
- [6] L. Zhang, W. G. Hurley, and W. H. Wölfe, "A new approach to achieve maximum power point tracking for PV system with a variable inductor," *IEEE Trans. Power Electron.*, vol. 26, no. 4, pp.1031-1037, Apr. 2011.
- [7] M. S. Perdigão, J. M. Alonso, M. A. Dalla Costa, and E. S. Saraiva, "Using magnetic regulators for the optimization of universal ballasts," *IEEE Trans. Power Electron.*, vol. 23, no. 6, pp. 3126-3134, Nov. 2008.
- [8] E. Orietti, P. Mattavelli, G. Spiazzi, C. Adragna, and G. Gattavari, "Two-phase interleaved LLC resonant converter with current controlled inductor," in Proc. Brazilian Power Electron. Conf., 2009, pp. 298-304.
- [9] M. S. Perdigão, M. F. Menke, A. R. Seidel, R. A. Pinto and J. M. Alonso, "A Review on Variable Inductors and Variable Transformers: Applications to Lighting Drivers," in *IEEE Transactions on Industry Applications*, vol. 52, no. 1, pp. 531-547, Jan.-Feb. 2016.
- [10] G. Martínez, J. M. Alonso and R. Osorio, "Analysis and Design of a Unidirectional Resonant Switched-Capacitor Step-Up Converter for OLED Lamp Driving Based on Variable Inductor," in *IEEE Journal of Emerging and Selected Topics in Power Electronics*, vol. 6, no. 3, pp. 1106-1115, Sept. 2018, doi: 10.1109/JESTPE.2018.2827324.
- [11] Y. Liu, H. A. Mantooth, J. Carlos Balda and C. Farnell, "A Variable Inductor Based LCL Filter for Large-Scale Microgrid Application," in *IEEE Transactions on Power Electronics*, vol. 33, no. 9, pp. 7338-7348, Sept. 2018, doi: 10.1109/TPEL.2017.2764483.
- [12] Y. Wei, Q. Luo, J. Wang and S. Pengju, "Analysis and design of the DCM operation boost PFC converter with magnetic control," in *IET Power Electronics*, vol. 12, no. 14, pp. 3697-3706, 27 11 2019, doi: 10.1049/iet-pel.2019.0437.
- [13] Y. Wei, Q. Luo, X. Du, N. Altin, J. M. Alonso and H. A. Mantooth, "Analysis and Design of the LLC Resonant Converter With Variable Inductor Control Based on Time-Domain Analysis," in *IEEE Transactions on Industrial Electronics*, vol. 67, no. 7, pp. 5432-5443, July 2020, doi: 10.1109/TIE.2019.2934085.
- [14] H. Fan and H. Li, "High-Frequency Transformer Isolated Bidirectional DC-DC Converter Modules with High Efficiency Over Wide Load Range for 20 kVA Solid-State Transformer," in *IEEE Transactions on Power Electronics*, vol. 26, no. 12, pp. 3599-3608, Dec. 2011.
- [15] Burgio, A.; Menniti, D.; Motta, M.; Pinnarelli, A.; Sorrentino, N.; Vizza, P., "A laboratory model of a dual active bridge DC-DC converter for a smart user network," in Environment and Electrical Engineering (EEEIC), 2015 IEEE 15th International Conference on, vol., no., pp.997-1002, 10-13 June 2015.
- [16] Y. Bi and D. C. Jiles, "Finite element modeling of an electrically variable inductor," in *IEEE Transactions on Magnetics*, vol. 35, no. 5, pp. 3517-3519, Sept. 1999.
- [17] M. S. Perdigão, S. F. Ferreira, M. Martins, A. S. Mendes and J. M. Alonso, "Finite element analysis of a variable inductor for an RSCC based LED lamp driver," 2015 IEEE Industry Applications Society Annual Meeting, Addison, TX, 2015, pp. 1-8.
- [18] D. C. Hamill, "Gyrator-capacitor modeling: a better way of understanding magnetic components," Proceedings of 1994 IEEE Applied Power Electronics Conference and Exposition - ASPEC'94, Orlando, FL, USA, 1994, pp. 326-332 vol.1.
- [19] Q. Chen, L. Xu, X. Ruan, S. C. Wong, and C. K. Tse, "Gyrator-Capacitor Simulation Model of Nonlinear Magnetic Core," in 2009 Twenty-Fourth Annual IEEE Applied Power Electronics Conference and Exposition, 2009, pp. 1740-1746.
- [20] J. M. Alonso, G. Martínez, M. Perdigão, M. Cosetin and R. N. do Prado, "Modeling magnetic devices using SPICE: Application to variable inductors," 2016 IEEE Applied Power Electronics Conference and Exposition (APEC), Long Beach, CA, 2016, pp. 1115-1122.
- [21] G. W. Ludwig and S.-A. El-Hamamsy, "Coupled inductance and reluctance models of magnetic components," *IEEE Trans. Power Electron.*, vol. 6, no. 2, pp. 240-250, Apr. 1991.
- [22] R. Prieto, R. Asensi, C. Fernandez, J. A. Oliver and J. A. Cobos, "Bridging the Gap Between FEA Field Solution and the Magnetic Component Model," in *IEEE Transactions on Power Electronics*, vol. 22, no. 3, pp. 943-951, May 2007.
- [23] Ferreira, Samuel Filipe Soares. Electromagnetic study of a variable inductor controlled by a DC current. MS thesis. University of Coimbra, 2016.
- [24] D. Medini and S. Ben-Yaakov, "A current-controlled variable inductor for high frequency resonant power circuits," in Proc. IEEE APEC, 1994, pp. 219-225.
- [25] S. Saeed, J. Garcia and R. Georgious, "Modeling of variable magnetic elements including hysteresis and Eddy current losses," 2018 IEEE Applied Power Electronics Conference and Exposition (APEC), San Antonio, TX, 2018, pp. 1750-1755.
- [26] Y. Hu, L. Huber and M. M. Jovanović, "Single-Stage, Universal-Input AC/DC LED Driver With Current-Controlled Variable PFC Boost Inductor," in *IEEE Transactions on Power Electronics*, vol. 27, no. 3, pp. 1579-1588, March 2012, doi: 10.1109/TPEL.2010.2082564.
- [27] A. P. Mendes, B. Baptista, M. S. Perdigão and A. M. S. Mendes, "Experimental analysis of a DC current-controlled variable inductor in a DC-DC converter," 2019 IEEE International Conference on Industrial Technology (ICIT), Melbourne, Australia, 2019, pp. 440-445, doi: 10.1109/ICIT.2019.8755161.
- [28] A. Van den Bossche and V. C. Valchev, *Inductors and Transformers for Power Electronics*, 2005.

- [29] W. J. Croisant, C. A. Feickert and M. K. McNerney, "A differential magnetic permeability model for pulsed magnetic field calculations," in IEEE Transactions on Magnetics, vol. 32, no. 5, pp. 4326-4328, Sept. 1996.
- [30] D. Zhang, Y. Zhou, P. Yan, T. Shao, and Y. Sun, "Differential permeability of ferrite cores at high magnetization rates," in 2010 IEEE International Power Modulator and High Voltage Conference, 2010, pp. 517-520.
- [31] M. Jaafar, V. Markovski, and M. Elleuch, "Modelling of the differential permeability and the initial magnetization curve for ferromagnetic materials," in 2004 IEEE International Conference on Industrial Technology, 2004. IEEE ICIT '04., 2004, vol. 1, pp. 460-465.
- [32] J. P. A. Bastos and N. Sadowski, "A New Formulation Using Differential Permeability Based on the Source-Field Method," IEEE Trans. Magn., vol. 46, no. 8, pp. 3369-3372, Aug. 2010.
- [33] J. P. A. Bastos, N. Sadowski, J. V. Leite, N. J. Batistela, K. Hoffmann, G. Meunier, and O. Chadebec, "A Differential Permeability 3-D Formulation for Anisotropic Vector Hysteresis Analysis," IEEE Trans. Magn., vol. 50, no. 2, pp. 341-344, Feb. 2014.
- [34] A. Van den Bossche, V. Valchev and T. Filchev, "Improved approximation for fringing permeances in gapped inductors," Conference Record of the 2002 IEEE Industry Applications Conference. 37th IAS Annual Meeting (Cat. No.02CH37344), Pittsburgh, PA, USA, 2002, pp. 932-938 vol.2.
- [35] Altair Flux™ [Online]. Available: <https://altairhyperworks.com/product/flux#>
- [36] Engauge Digitizer Software [Online]. Available: <http://markummitchell.github.io/engauge-digitizer>, last Accessed: July 17, 2020.
- [37] Ferrites and accessories, TDK [Online]. Available: <https://www.tdk-electronics.tdk.com/download/528882/71e02c7b9384de1331b3f625ce4b2123/pdf-n87.pdf>
- [38] S. Saeed, R. Georgious, J. Garcia, "Modeling of Magnetic Elements Including Losses—Application to Variable Inductor," *Energies* 2020, 13, 1865.
- [39] J. M. Alonso, M. Perdigão, M. A. Dalla Costa, S. Zhang and Y. Wang, "Variable inductor modeling revisited: The analytical approach," *2017 IEEE Energy Conversion Congress and Exposition (ECCE)*, Cincinnati, OH, 2017, pp. 895-902, doi: 10.1109/ECCE.2017.8095880.
- [40] P. L. Dowell, "Effects of eddy currents in transformer windings," in *Proceedings of the Institution of Electrical Engineers*, vol. 113, no. 8, pp. 1387-1394, August 1966, doi: 10.1049/piee.1966.0236.
- [41] George G. Orenchak, Estimating Temperature rise of transformers [Online]. Available: <http://www.tscinternational.com/tech12.pdf>
- [42] S. S. Ben-Yaakov, "SPICE simulation of ferrite core losses and hot spot temperature estimation," *2017 24th IEEE International Conference on Electronics, Circuits and Systems (ICECS)*, Batumi, 2017, pp. 107-110, doi: 10.1109/ICECS.2017.8292005.
- [43] S. Saeed, R. Georgious, and J. Garcia, "Modeling of Magnetic Elements Including Losses—Application to Variable Inductor," *Energies*, vol. 13, no. 8, p. 1865, Apr. 2020.
- [44] J. Reinert, A. Brockmeyer, and R. W. A. A. De Doncker, "Calculation of losses in ferro- and ferrimagnetic materials based on the modified steinmetz equation," IEEE Transactions on Industry Applications, vol. 37, no. 4, pp. 1055-1061, 2001.
- [45] Jieli Li, T. Abdallah, and C. R. Sullivan, "Improved calculation of core loss with nonsinusoidal waveforms," in Conference Record of the 2001 IEEE Industry Applications Conference. 36th IAS Annual Meeting (Cat. No.01CH37248), vol. 4, 2001, pp. 2203-2210 vol.4.
- [46] K. Venkatachalam, C. R. Sullivan, T. Abdallah, and H. Tacca, "Accurate prediction of ferrite core loss with nonsinusoidal waveforms using only steinmetz parameters," in 2002 IEEE Workshop on Computers in Power Electronics, 2002. Proceedings., 2002, pp. 36-41.
- [47] M. W. Beraki, J. P. F. Trovão, M. S. Perdigão and M. R. Dubois, "Variable Inductor Based Bidirectional DC-DC Converter for Electric Vehicles," in *IEEE Transactions on Vehicular Technology*, vol. 66, no. 10, pp. 8764-8772, Oct. 2017, doi: 10.1109/TVT.2017.2710262.